

rf Quantum Capacitance of the Topological Insulator Bi_2Se_3 in the Bulk Depleted Regime for Field-Effect Transistors

A. Inhofer,¹ J. Duffy,^{2,3} M. Boukhicha,¹ E. Bocquillon,¹ J. Palomo,² K. Watanabe,⁴ T. Taniguchi,⁴ I. Estève,⁵ J. M. Berroir,¹ G. Fève,¹ B. Plaçais,¹ and B. A. Assaf²

¹Laboratoire Pierre Aigrain, Département de Physique, Ecole Normale Supérieure, PSL Research University, Université Paris Diderot, Sorbonne Paris Cité, Sorbonne Université, CNRS, 24 rue Lhomond, 75005 Paris, France

²Département de Physique, Ecole Normale Supérieure, PSL Research University, CNRS, 24 rue Lhomond, 75005 Paris, France

³Chemical Engineering Department, Northeastern University, 360 Huntington Avenue, Boston, Massachusetts 02115, USA

⁴National Institute for Materials Science, 1-1 Namiki, Tsukuba, Ibaraki 305-0044, Japan

⁵Institut de Minéralogie, de Physique des Matériaux et de Cosmochimie, UMR 7590 CNRS UPMC-IRD-MNHN, Campus Jussieu, 4 Place Jussieu, 75005 Paris, France



(Received 8 September 2017; revised manuscript received 15 December 2017; published 22 February 2018)

A metal-dielectric topological-insulator capacitor device based on hexagonal-boron-nitrate- (*h*-BN) encapsulated CVD-grown Bi_2Se_3 is realized and investigated in the radio-frequency regime. The rf quantum capacitance and device resistance are extracted for frequencies as high as 10 GHz and studied as a function of the applied gate voltage. The superior quality *h*-BN gate dielectric combined with the optimized transport characteristics of CVD-grown Bi_2Se_3 ($n \sim 10^{18} \text{ cm}^{-3}$ in 8 nm) on *h*-BN allow us to attain a bulk depleted regime by dielectric gating. A quantum-capacitance minimum and a linear variation of the capacitance with the chemical potential are observed revealing a Dirac regime. The topological surface state in proximity to the gate is seen to reach charge neutrality, but the bottom surface state remains charged and capacitively coupled to the top via the insulating bulk. Our work paves the way toward implementation of topological materials in rf devices.

DOI: [10.1103/PhysRevApplied.9.024022](https://doi.org/10.1103/PhysRevApplied.9.024022)

I. INTRODUCTION

Topological phases of matter have emerged as a fundamental paradigm in the study of condensed matter physics [1–4]. Topological insulators (TIs) are essentially material realizations that stem from this theoretical paradigm [4–8]. They are interesting from both the fundamental and applied perspectives. Typically, a topological insulator is a material that has an inverted orbital band ordering in the 3D bulk, which leads to the existence of Dirac cones at the surface of the material at symmetric points in the Brillouin zone [4,5]. These Dirac fermions are spin-momentum locked and highly robust to backscattering. From the fundamental perspective, a number of states of matter have so far been realized in topological insulators. The quantum anomalous Hall state [9,10], the Majorana fermion [11], and the quantized Faraday and Kerr effects [12,13] are examples of such realizations. From the applied perspective, implementation in spintronic data-storage devices and high-frequency transistors is envisaged. Highly efficient spin-torque switching and spin injection have already been demonstrated in ferromagnet-TI bilayer devices, thus, establishing potential use in data storage [14–16]; however,

studies aimed to realize high-frequency transistors are still lacking.

An important step to realize high-frequency transistors is to characterize the capacitive response of the TI at radio frequency (rf) and establish its Dirac-like nature. The rf-transport regime has already been significantly studied in graphene [17–20] and more recently in HgTe TIs [21,22]. In this regime, one can simultaneously measure the quantum capacitance of the Dirac states and the conductivity of the material. Contrary to the constant capacitance-voltage characteristic typical of metal-insulator-metal capacitors [Fig. 1(a)], in metal-insulator-graphene and metal-insulator-topological-insulator capacitors (MITI CAP), the capacitance is a function of the applied voltage [Fig. 1(b)]. The quantum capacitance being related to the compressibility or the density of states then allows one to directly measure those quantities [17]. This is, however, only possible for materials that have a low carrier density and good mobility. For this particular reason, rf capacitance studies have remained highly challenging in Bi-based 3D TIs. In the case of Bi_2Se_3 , for example, residual bulk n doping renders a reliable detection of surface-state signatures difficult [23–25]. The first step in realizing a rf-transport

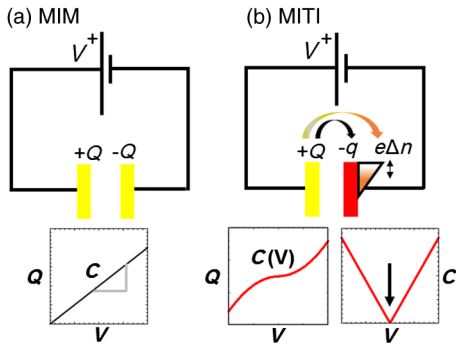


FIG. 1. (a) Linear charge (Q) vs voltage (V) characteristic of a metal-insulator-metal (MIM) device. The capacitance is constant in this case. (b) Nonlinear Q vs V curve characteristic of voltage-dependent quantum capacitance in a MITI CAP. The quantum capacitance is due to the finite change in density ($e\Delta n$) and chemical potential at the surface of the TI. The arrow in the C - V graph indicates the Dirac point.

device based on Bi_2Se_3 is a solution to the issue of material quality.

Motivated by recent positive results on the growth of Bi_2Se_3 by chemical vapor deposition (CVD) on mechanically exfoliated hexagonal boron nitride (h -BN) [26,27], we undertake a similar procedure. We first grow Bi_2Se_3 by CVD on high-quality h -BN [28,29] and then transfer a second layer of h -BN on top of the grown Bi_2Se_3 to realize a capacitor device. The excellent dielectric properties of the h -BN used in this work and the improved transport characteristics of CVD-grown Bi_2Se_3 on h -BN allow us to observe clear signatures of Dirac surface states in the rf-transport regime. We are able to simultaneously measure both the quantum capacitance and the channel resistance of the device. The capacitance exhibits a linear variation and a minimum versus chemical potential characteristic of Dirac fermions. The resistance shows a strong increase with decreasing voltage in the depleted regime. It does not reach

a maximum at the capacitance dip. We argue that this is due to the contributions of the bottom surface in the bipolar regime. Our work provides a quantitative analysis of the compressibility of Bi_2Se_3 in the rf regime and establishes the Dirac nature of the rf response in TIs.

II. GROWTH AND CHARACTERIZATION

Bi_2Se_3 nanoflakes are grown by catalyst-free CVD using a three-zone tube furnace following a procedure similar to what is reported by Xu *et al.* [26]. All growths are performed on high-resistivity Si/SiO_2 substrates having an oxide thickness of 300 nm, on which we mechanically exfoliate h -BN. The furnace tube is initially pumped down to 8×10^{-2} mbar. A powder source of high-purity (99.99%) Bi_2Se_3 is placed in the hot zone (A) of the furnace in a stream of argon gas (99.999%) flowing at 200 sccm [Fig. 2(a)]. The substrate [Fig. 2(b)] is placed downstream from the source in the colder zone (B). Zones (A) and (B) are initially heated to 300°C in 30 min. (A) is then heated to 600°C while (B) is heated only to 400°C in 30 min. These temperatures are maintained for 60 s. Both zones are finally cooled to 200°C in 80 min. An absolute pressure of 3.9 mbar is maintained during the entire process.

An optical microscope image of a characteristic sample is shown in Figs. 2(b) and 2(c) before and after the growth, respectively. A layer of Bi_2Se_3 is seen to coat the h -BN flakes, but it does not nucleate on the SiO_2 . The Z-contrast scanning electron microscope image shown in Fig. 2(d) confirms nucleation of Bi_2Se_3 on the h -BN flake. The dark spots observed on the light gray flake indicate the presence of heavy atoms such as Bi or Se. This growth mechanism is consistent with the previous reports on CVD synthesis of Bi-based TI on h -BN [26,27].

Figure 2(e) shows Raman spectra obtained using an excitation wavelength of 532 nm on Bi_2Se_3 flakes having thicknesses ranging from 2 to 90 quintuple layers (QLs). The thinnest flakes studied in Raman spectroscopy (2–4

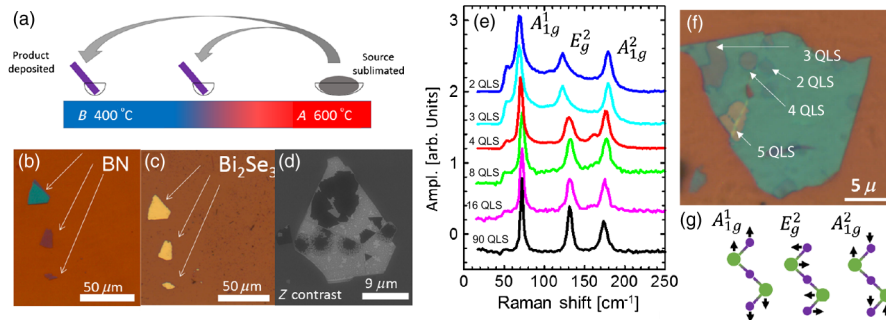


FIG. 2. (a) Schematic of the CVD growth tube showing the Bi_2Se_3 source in hot zone A and substrates in colder zone B downstream in the argon flow direction. (b) Optical microscopy image showing h -BN-exfoliated flakes on SiO_2 prior to growth. (c) The same h -BN flakes coated with 90 QLs of Bi_2Se_3 after the growth. (d) Z-contrast SEM image of Bi_2Se_3 growth (dark patches) on a h -BN flake. (e) Microscopic Raman spectroscopy of Bi_2Se_3 flakes of different thicknesses on h -BN. The (2–4)-QL flakes are shown in (f). Three Raman active peaks are observed in (e) corresponding to the three vibrational modes shown in (g), namely, the A_{1g}^1 and A_{1g}^2 out-of-plane modes and the E_g^2 in-plane mode.

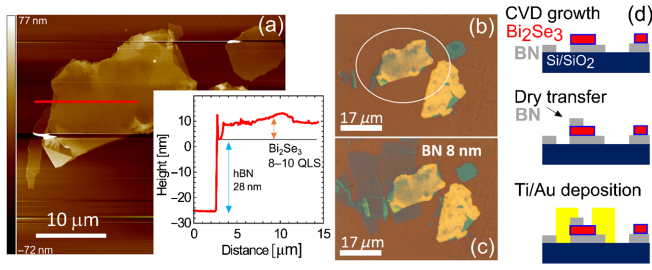


FIG. 3. (a) AFM image of a selected 8-QL-thick Bi_2Se_3 flake. Inset shows the height as a function of the distance measured along the red line shown in the AFM image. The Bi_2Se_3 is 8–10 QL thick, and the underlying $h\text{-BN}$ is 28 nm thick. (b) Optical microscope image of the flake shown in (a). (c) 8-QL Bi_2Se_3 flake with an 8-nm $h\text{-BN}$ flake transferred on top using the dry-transfer method. (d) Summary of the device processing steps: growth of exfoliated BN and dry transfer of top BN and Ti/Au metal deposition.

QLs) all nucleate on the same BN flake shown in Fig. 2(f). Three characteristic Raman active phonon peaks [Fig. 2(g)] are observed in Fig. 2(e) between 50 and 200 cm^{-1} , confirming the presence of a Bi_2Se_3 layer on the exfoliated $h\text{-BN}$. A blueshift of the A_{1g}^2 mode and a redshift of the E_g^2 and A_{1g}^1 modes are observed with decreasing thickness, in agreement with previous reports on Raman spectroscopy on Bi_2Se_3 [26,30].

III. DEVICE FABRICATION

Three flakes (6, 8, 13 QLs) having different thicknesses obtained from identical growths are selected for device implementation. The 8-QL sample is studied in detail. The results from the other three samples are shown in the Appendix. An AFM image of the 8-QL sample is shown in Fig. 3(a). We measure the Bi_2Se_3 thickness across the line shown in the inset of Fig. 3(a). We find a thickness varying between 8 and 10 QLs. A small peak-to-peak surface

roughness of 1–2 QLs is detected. A $h\text{-BN}$ flake is then transferred on top of the grown Bi_2Se_3 using the standard dry-transfer method already proven successful for graphene [31,32] and 2D semiconductors [33–37]. Optical images of the sample are shown in Figs. 3(b) and 3(c) before and after the transfer, respectively. The transfer is performed in air, therefore, exposing the top surface of Bi_2Se_3 to the atmosphere. The transferred $h\text{-BN}$ layer is chosen to be thinner than 10 nm (8 nm in this case), in order to maximize its geometric capacitance and render the quantum capacitance of the Bi_2Se_3 experimentally visible. A single $e\text{-beam}$ lithography step then allows us to pattern the gate and drain electrodes, as well as a coplanar waveguide. A metallic bilayer of Ti(5 nm)/Au(150 nm) is then deposited. Note that prior to depositing the Ti layer, light argon etching (<10 s) is performed *in situ* to remove any native oxides and to minimize contact resistance. The device processing sequence is summarized in Fig. 3(d). The $h\text{-BN}$ -encapsulated Bi_2Se_3 capacitor device embedded in a rf waveguide is shown Figs. 4(a) and 4(b).

IV. rf-TRANSPORT MEASUREMENTS

The devices are characterized using rf-transport measurements for frequencies between 0.03 and 10 GHz using a variable network analyzer in a cryogenic rf-probe station, as detailed in our previous work [17,21,22]. A standard short-open-load-through calibration is performed before the measurement. The S -matrix components are extracted by measuring the reflected and transmitted wave intensity through the device as a function of the frequency for different gate voltages using a variable network analyzer. The complex admittance (inverse impedance) is then extracted from the S -matrix components. The real and imaginary parts of the device admittance are quantified versus the frequency and gate voltage. Proper care is taken to deembed [38] parasitic capacitive and inductive contributions resulting from the device geometry by measuring

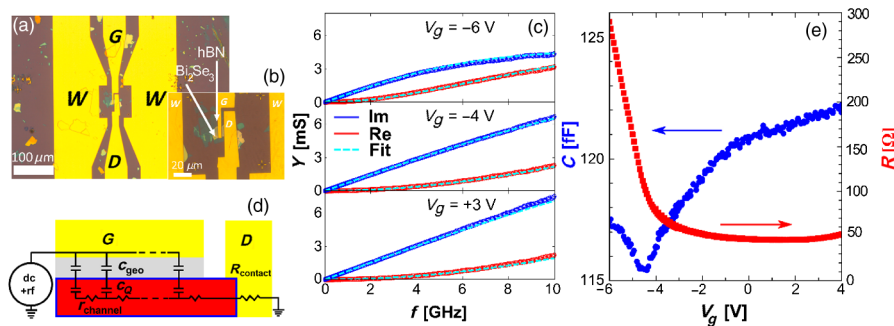


FIG. 4. (a) Optical microscope image of the finished device with the capacitor shown embedded inside a coplanar waveguide (W). G and D denote the gate and drain contacts, respectively. (b) Enlarged microscope image showing the capacitor device. (c) Real (red) and imaginary (blue) parts of the rf admittance as a function of the frequency for three typical gate voltages. (d) Schematic of a distributed RC -line model in series with a contact resistance. The capacitance is split into two components: the geometric capacitance C_{geo} and the quantum capacitance C_Q . (e) Total device capacitance and channel resistance extracted by fitting the model corresponding to the circuit shown in (d) to the data in (c). Curve fits in (c) are shown as dashed lines.

a dummy device having identical contact geometry without the Bi_2Se_3 flake in between, as well as a conductive through-line. Such measurements also rule out any parasitic rf signals stemming from the substrate Si/SiO_2 substrates. All measurements are made at 10 K. In what follows, we focus on the measurements of the 8-QL device shown in Figs. 3 and 4.

The deembedded sample admittance versus frequency is shown in Fig. 4(c) for three different gate voltages. The data are then fit using a distributed RC -line model (of admittance Y_{RC}) in series with a contact resistance R_{contact} [Fig. 4(d)] similar to what was previously reported for graphene [17]. The total admittance Y_{total} is given by

$$Y_{\text{total}}(\omega) = \frac{1}{Y_{RC}^{-1}(\omega) + R_{\text{contact}}}, \quad (1)$$

where

$$Y_{RC} = j\omega CLw \frac{\tanh(L\sqrt{j\omega C}/\sigma)}{L\sqrt{j\omega C}/\sigma}. \quad (2)$$

Here, $\omega = 2\pi f$ is the frequency, $j = \sqrt{-1}$, and $L = 4.3 \mu\text{m}$ and $w = 12.8 \mu\text{m}$ are the device length and width, respectively. σ is the channel conductivity. C is the total device capacitance

$$C^{-1} = c_{\text{geo}}^{-1} + c_Q^{-1}, \quad (3)$$

where c_{geo} is the geometric capacitance, and $c_Q = e^2\chi$ is quantum capacitance related to the compressibility $\chi = [(\partial n)/(\partial \epsilon_F)]$. Here, ϵ_F represents the chemical potential at the sample surface, and n is a 2D carrier density.

The curve fit of $Y_{\text{total}}(\omega)$ allows us to separate C and σ for different gate voltages. As seen in Fig. 4(c), the model yields an excellent fit to the data up to 10 GHz. The results for C and R from curve fits up to 10 GHz are shown in Fig. 4(e) as a function of the gate voltage between -6 and 1 V. The capacitance decreases progressively for decreasing voltage (0 to -5 V), goes through a minimum at about -5 V, and then increases again between -5 and -6 V. With a capacitance dip of 5%, our results agree with previous low-frequency capacitance measurements of similar Bi_2Se_3 reporting a capacitance dip of 6% [26].

The resistance exhibits a continuous increase that accelerates near the capacitance minimum. No resistance maximum is observed. A fixed contact resistance $R_c \approx 20 \Omega$ is included in the curve fit to the admittance data. Allowing this contact resistance to vary yields negligible variation compared to the fivefold increase observed in the channel resistance. We can, thus, confidently claim that our two-point rf measurement yields a reliable simultaneous measurement of the quantum capacitance and channel resistance.

V. ANALYSIS OF THE QUANTUM CAPACITANCE OF TOP-SURFACE STATES

We next focus on the analysis of quantum capacitance. c_Q can be extracted using Eq. (3) by fixing $c_{\text{geo}} = (124 \pm 1)$ fF, the value at which the capacitance is seen to saturate in Fig. 4(e). The measured geometric capacitance is slightly lower than what is expected for h -BN having $\kappa = 3.2$, possibly as a result of the rough surface of Bi_2Se_3 . The capacitance per unit area c_Q is then determined by dividing the capacitance by the geometrical factors L and w . c_Q is shown in Fig. 5(a). The gray lines in Fig. 5(a) delimit the propagated uncertainty on c_Q due to the uncertainty associated with c_{geo} . A powerful consequence of our measurements is the fact that they allows us to determine the local (top surface) chemical potential ϵ_f directly from experimental data via the Berglund integral without *a priori* knowledge of the band structure. The Berglund integral is written as [39]

$$\epsilon_f = \int_0^{V_g} dV \left(1 - \frac{C(V)}{c_{\text{geo}}} \right). \quad (4)$$

We use Eq. (4) to extract ϵ_f , which we now plot as a function of V_g in Fig. 5(b) along with the propagated uncertainty associated with it. We can now plot the quantum capacitance c_Q versus the local chemical potential ϵ_f . This is shown in Fig. 5(c). The minimum in c_Q defines the chemical potential origin, as it is associated with the position of the Dirac point; and allows us to determine the Fermi energy at zero applied potential to be close

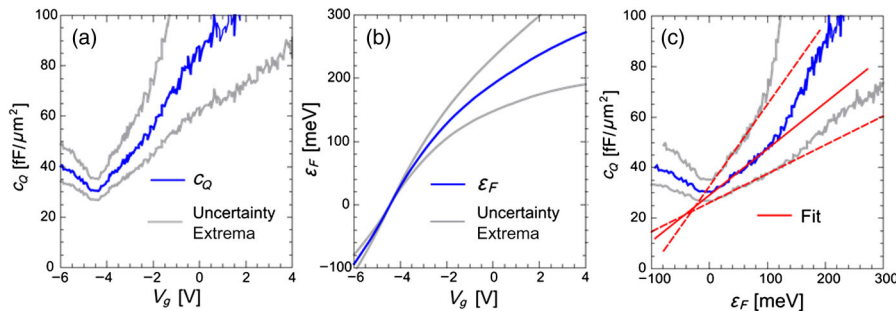


FIG. 5. (a) Quantum capacitance versus gate voltage at 10 K. (b) Surface chemical potential (Fermi energy) versus gate voltage. (c) Quantum capacitance versus Fermi energy. Blue line represents data, gray lines show uncertainty extrema, red lines are linear fits using Eq. (5).

TABLE I. Comparison of the Bi₂Se₃ sample studied in this work to those previously reported.

At $V_g = 0$	n_{sheet} (cm ⁻³)	Thickness QL	Type of sample
This work	2×10^{18}	8	CVD
Ref. [45]	4×10^{19}	80	CVD
Ref. [48]	4×10^{19}	100	CVD
Ref. [49]	$(1-3) \times 10^{18}$	10	MBE
Ref. [50]	$(5-10) \times 10^{18}$	10	MBE
Ref. [46]	$(1-2) \times 10^{19}$	10	MBE
Ref. [47]	7×10^{19}	10	MBE
Ref. [44]	2×10^{19}	20	MBE
Ref. [42]	2×10^{19}	8	MBE
Ref. [51]	$>10^{19}$	10 QLs pristine	Exfoliated

to (200 ± 40) meV above the Dirac point. This Fermi energy corresponds to a surface Dirac carrier density of $(3 \pm 1) \times 10^{12}$ cm⁻². Assuming the Dirac point occurs at 200 meV below the bottom-most bulk conduction band, as seen in ARPES [23,40], we get a Fermi-level position of, at most, 40 meV above the conduction-band bottom of Bi₂Se₃ (assumed parabolic with $m^* = 0.14m_0$) [41]. This Fermi-level position yields a slight native bulk n doping of 2×10^{18} cm⁻³. This is a significant improvement compared to pristine quality Bi₂Se₃ where typically $n > 10^{19}$ cm⁻³ [42–47] and agrees with previous reports on improved quality samples (see Table I) [48,49].

We can additionally perform a linear fit to the c_Q versus ε_f curve. This is shown as the solid red line fit to the data in Fig. 5(c). The dashed lines are fit extrema to the edges of the shaded area and allow us to determine the uncertainty on the extracted slope. The slope allows us to extract the Dirac velocity of the topological surface states near the Dirac point, from the expression of the compressibility χ , which is related to c_Q :

$$c_Q = e^2 \chi = \frac{e^2 \varepsilon_f}{2\pi(\hbar v_f)^2}. \quad (5)$$

We find a Dirac velocity equal to $(5.8 \pm 1.4) \times 10^5$ m/s. This agrees within experimental uncertainty with previously reported velocities that vary between 5×10^5 and 4.5×10^5 m/s [25,40,52]. It is worthwhile highlighting that while we can perfectly account for the variation of the quantum capacitance versus Fermi energy shown in Fig. 5(c), this analysis cannot account for the finite c_Q offset observed at the minimum. From Eq. (5), it is evident that c_Q should go to zero at $\varepsilon_f = 0$. The typical capacitance offset at the Dirac point observed in graphene, for example, is an order of magnitude lower than what is observed here [53]. Our data suggest the presence of additional capacitive contributions in parallel with that of the top Dirac surface states. A thorough understanding of these capacitive

contributions from other transport channels must, thus, be provided.

VI. THE ORIGIN OF THE CAPACITANCE OFFSET: CAPACITIVE COUPLING OF TOP AND BOTTOM SURFACE CHANNELS

First, it is simple to rule out reminiscent bulk carriers as the source of this offset simply by computing the screening length for Bi₂Se₃ using the measured quantum capacitance. In order to extract the screening length from experimental data, we need to develop an expression that relates the screening length to the 2D density of states and to the quantum capacitance. This is discussed in detail in Appendix A. The end result is a screening length that scales linearly with the inverse of the 2D quantum capacitance of bulk states c_Q^{bulk} :

$$\lambda = \frac{\kappa \varepsilon_0}{c_Q^{\text{bulk}}}. \quad (6)$$

Note that here, c_Q^{bulk} is a quantum capacitance related to a surface charge accumulation or depletion that screens the electric field over a finite length. $\kappa \approx 100$ is the generally accepted static dielectric constant of Bi₂Se₃ [50,51,54–56]. $\varepsilon_0 = 8.85 \times 10^{-12}$ F/m is the permittivity of free space. If we assume that all measured quantum-capacitance contributions are due to screening, then for $c_Q^{\text{bulk}} < 100$ fF/ μm^2 , λ exceeds 10 nm and the thickness of the sample (8 nm), implying that full bulk depletion is possible. Near the capacitance minimum, it is, thus, highly unlikely that reminiscent charge carriers from the bulk contribute to the transport.

Consequently, we can consider the situation of a fully depleted insulating bulk that contributes a geometric capacitance between two metallic surfaces. The Dirac character of the top metallic surface is proven by the quantum capacitance observed in Fig. 5. However, the character of the bottom surface is not evident in our experiments. Experimentally, we can still determine the net quantum-capacitance contribution of this bottom metallic layer, assuming it couples capacitively in parallel with the top surface via the insulating bulk:

$$c_Q = c_Q^{\text{TTSS}}(\varepsilon_f) + \left(\frac{1}{c_g^{\text{bulk}}} + \frac{1}{c_Q^{\text{bottom}}(\varepsilon_f)} \right)^{-1}. \quad (7)$$

Here, ε_f denotes the chemical potential of the top surface, c_Q^{TTSS} is top-surface quantum capacitance, and c_Q^{bottom} is that of the bottom metallic surface. The geometric capacitance of the insulating bulk with a thickness $d_{\text{Bi}_2\text{Se}_3} \approx 8$ nm is given by

$$c_g^{\text{bulk}} = \frac{\kappa \varepsilon_0}{d_{\text{Bi}_2\text{Se}_3}} \approx 110 \text{ fF}/\mu\text{m}^2. \quad (8)$$

When $c_Q^{\text{TTSS}}(\varepsilon_f = 0) = 0$, an offset equal to (30 ± 5) fF/ μm^2 has to result from the other term in

Eq. (7). Equations (7) and (8) yield $c_Q^{\text{bottom}} = (40 \pm 10) \text{ fF}/\mu\text{m}^2$. It can be easily shown that the quantum capacitance expected from a quadratically dispersing Bi_2Se_3 interfacial 2DEG significantly exceeds this value

$$\frac{\hbar^2 \pi}{e^2 m^*} = \frac{94 \text{ fF}}{\mu\text{m}^2} > c_Q^{\text{bottom}}$$

using the effective mass of Bi_2Se_3 , $m^* = 0.14m_0$ [41]. This is, therefore, an unlikely scenario.

The last scenario to consider is when the bottom Dirac TSS having a finite Fermi energy at the charge neutrality point of the top TSS yields the offset in the quantum capacitance. Using Eq. (5), we estimate for a chemical potential close to $(170 \pm 40) \text{ meV}$ above the Dirac point (with $v_f \approx 5 \times 10^5 \text{ m/s}$), a Dirac quantum capacitance $c_Q^{\text{bottom}} = (40 \pm 10) \text{ fF}/\mu\text{m}^2$. We conclude that the most likely explanation for the observed offset is the presence of the bottom TSS that couples capacitively to the top TSS via the insulating bulk.

VII. CHARGING CURVE OF A BULK DEPLETED TOPOLOGICAL INSULATOR

In order to get further insight into the charging mechanism expected in such a situation, we develop in Figs. 6(a) and 6(b) a model that describes the charging of both the top and bottom TSS coupled via the bulk as a function of the top gate voltage. This capacitance model is summarized by the circuit shown in Fig. 6(b). The total quantum capacitance corresponding to this circuit is given by Eq. (7).

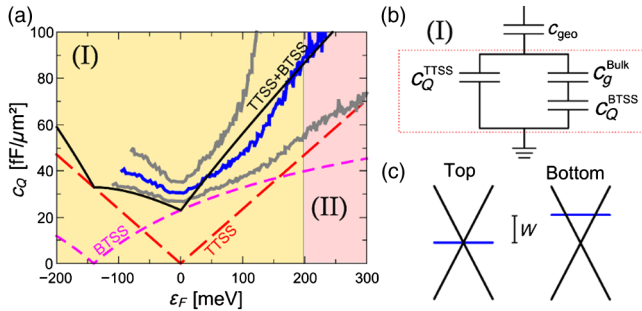


FIG. 6. (a) Quantum capacitance versus surface chemical potential data (blue) compared to the model of the topological insulator shown in (b). Gray curves represent the upper and lower bounds of the experimental data, the black solid line is the total quantum capacitance resulting from this model, the dashed red line is that of the top TSS, and the dashed magenta line is that of the bottom TSS. (b) MITI CAP model of a topological insulator in the bulk depleted regime where the top TSS (c_Q^{TTSS}) is capacitively coupled to the bottom TSS (c_Q^{BTSS}) via the insulating bulk assumed to have a geometrical capacitance (c_g^{bulk}). (c) Top and bottom Dirac surface states with respective chemical potential. W is the chemical potential offset. The bottom TSS remains filled when the top TSS is at charge neutrality.

The quantum capacitance of the top TSS c_Q^{TTSS} is computed using Eq. (5) with $v_f \approx 5 \times 10^5 \text{ m/s}$ [25]. Note that in Eq. (7), ϵ_f is the top-surface chemical potential. Hence, the expression for that of the bottom TSS $c_Q^{\text{bottom}}(\epsilon_f)$ is not simply given by Eq. (5). We show in the Appendix that the effective capacitance of the bottom TSS that is capacitively coupled via the insulating bulk is given by

$$\left(\frac{1}{c_g^{\text{bulk}}} + \frac{1}{c_Q^{\text{BTSS}}(\epsilon_f)} \right)^{-1} = c_g^{\text{bulk}} \left[1 - \frac{1}{\left(\sqrt{1 + \frac{e^2 |\epsilon_f + W|}{\pi (\hbar v_f)^2 c_g^{\text{bulk}}} \right)} \right], \quad (9)$$

where $c_Q^{\text{BTSS}}(\epsilon_f)$ is the bottom TSS Dirac quantum capacitance as a function of the top-surface chemical potential. W is the band offset between the top and bottom TSS. It is the only adjustable parameter in the model. The W term allows the top and bottom TSS to have a different local chemical potential [Fig. 6(c)], as has been reported in previous studies [57,58].

The contribution of c_Q^{TTSS} is shown in red in Fig. 6(a). The evolution of the effective capacitance of the bottom TSS c_Q^{BTSS} in series with the insulating bulk as a function of top-surface chemical potential ϵ_f is shown in dashed magenta. For $W \approx 140 \text{ meV}$, Eq. (9) is in good agreement with the data, as seen in Fig. 6(a). The quantum capacitance associated to the bottom surface is seen to flatten out at large values of ϵ_f due to an enhanced screening of the electric field at large charge carrier density by the top TSS. Note that this treatment is only valid when the bulk is fully depleted [region I in Fig. 6(a)]; the quantum capacitance from populated bulk bands should be taken into account at larger Fermi energies [region II in Fig. 6(a)]; however, our data are not precise enough to provide any quantitative analysis in this region.

We, thus, show that the measured quantum capacitance can be reliably explained by a model of two capacitively coupled Dirac surface states. Such a strong bottom TSS contribution to the compressibility has been disregarded in HgTe samples studied previously [21,59]. It becomes important here due to the large permittivity, the large band gap, and the nanometric thickness of the Bi_2Se_3 crystals grown by CVD. Importantly, for top-surface chemical potentials ϵ_f between 0 and about -140 meV , the top and bottom surfaces have different carrier polarity, i.e., p type and n type, respectively.

VIII. THE BEHAVIOR OF THE CHANNEL RESISTANCE

Next, we qualitatively discuss the variation of the channel resistance. Near the capacitance minimum, a fast increase in the channel resistance is observed, likely corresponding to the depletion of surface carriers on the

top and bottom surfaces, but no resistance maximum is reached. Since the Fermi energy is likely higher above the Dirac point at the bottom surface, bottom Dirac electrons provide a parallel conduction channel that has a much lower resistivity. The effective resistance from both top and bottom parallel channels is, hence, dominated by the resistivity of the bottom channel. Therefore, one does not expect to observe an ambipolar resistance maximum as long as the bottom Dirac cone remains heavily occupied.

Lastly, going up in Fermi energy away from the capacitance minimum, the resistance curve flattens out and eventually increases at large positive values of V_g [Fig. 4(e)]. We point out that this increased scattering at high charge carrier density in the top TSS is likely associated to subband scattering as reported in Refs. [21,22]. It is worth noting that any issue with the contact resistance can be ruled out. First, the Au/Bi₂Se₃ interface is not under the gate stack and, therefore, remains Ohmic throughout the entire experiment since Bi₂Se₃ remains *n* doped away from the gate stack. Second, even when the top surface is very close to neutrality, the bottom surface of the sample remains carrier doped, thus, ensuring a good connection with the source contact. This highlights the strength of our measurement and the local nature of the quantum capacitance in our experiment.

IX. CONCLUSION

In conclusion, we realize implementation of CVD-grown Bi₂Se₃ in rf capacitor devices and report the observation of the quantum capacitance of the top Dirac surface state and its variation versus the gate voltage. The reduced electron doping of Bi₂Se₃ grown in these conditions and the use of a high-quality *h*-BN dielectric allows us to quantify the quantum capacitance of Bi₂Se₃ and observe its minimum resulting from the top topological surface Dirac point. A detailed analysis of the field-effect mechanism in thin Bi₂Se₃ flakes shows that a bulk depleted regime can be reached at an accessible gate voltage in *h*-BN-encapsulated Bi₂Se₃ allowing us to investigate Dirac physics. We lastly model the capacitance-voltage curve of a TI slab consisting of two surface states separated by an insulating bulk and confirm its correspondence with our data. As an outlook, a dual-gated device might allow us to electrostatically compensate the chemical-doping asymmetry between the two surfaces [57]. Topological materials with even larger dielectric constants will also be interesting to investigate [60,61]. Overall, our work establishes *h*-BN-encapsulated Bi₂Se₃ as a promising platform to motivate future work on implementation in high-frequency transistors.

ACKNOWLEDGMENTS

We acknowledge Michael Rosticher's valuable assistance with the cleanroom equipment and Pascal Morfin for his assistance with the growth equipment setup. We also

acknowledge discussions with H. Graef. B. A. A. and J. D. acknowledge funding from ANR-LabEx ENS-ICFP Grant No. ANR-10-LABX-0010/ANR-10-IDEX-0001-02PSL. J. D. is partially supported by the Northeastern University Coop fellowship. The SEM facility of the Institut de Minéralogie et de Physique des Milieux Condensés is supported by Région Ile-de-France SESAME 2006 Grant No. I-07-593/R, INSU-CNRS, INP-CNRS, University Pierre et Marie Curie-Paris 6, and by the French National Research Agency Grant No. ANR-07-BLAN-0124-01. Growth of hexagonal boron nitride crystals is supported by the Elemental Strategy Initiative conducted by the MEXT, Japan and JSPS KAKENHI Grant No. JP15K21722.

APPENDIX A: QUANTUM CAPACITANCE AND DIELECTRIC SCREENING OF AN ELECTRON-DOPED 3D SEMICONDUCTOR

The quantum capacitance is directly related to the compressibility—the variation of the 2D electrical charge density per unit chemical potential $[(\partial n_{2D})/\partial \mu_T]$:

$$c_Q = e^2 \frac{\partial n_{2D}}{\partial \mu_T} = e^2 \frac{\partial}{\partial \mu_T} \left[\int_0^d \frac{\rho(z)}{e} dz \right]. \quad (\text{A1})$$

Here, n_{2D} is the surface carrier density, $\mu_T \equiv \epsilon_F$ is the top-surface chemical potential, and $\rho(z)$ the 3D charge density. The z axis is chosen to be perpendicular to the surface of the material and, therefore, parallel to the electric field. The top BN-Bi₂Se₃ interface is at $z = 0$.

From the conservation of electrochemical potential, we get $\mu_T = -eV_0$.

$V_0 = V(z = 0)$ is the electric potential at the dielectric semiconductor interface. The quantum capacitance can then be written as

$$c_Q = e^2 \frac{\partial n_{2D}}{\partial \mu_T} = -\frac{\partial}{\partial V_0} \left[\int_0^\infty \rho(z) dz \right].$$

Poisson's law relates the charge to the electric potential

$$\rho(z) = \kappa \epsilon_0 \frac{\partial^2 V}{\partial z^2},$$

where κ is the dielectric constant, and $\epsilon_0 = 8.85 \times 10^{-12}$ F/m is the permittivity of free space.

Plugging the expression for the charge density into c_Q and performing the integration gives

$$c_Q = -\kappa \epsilon_0 \frac{\partial}{\partial V_0} \left(\left[\frac{\partial V}{\partial z} \right]_{z \rightarrow \infty} - \left[\frac{\partial V}{\partial z} \right]_{z=0} \right).$$

We assume $[(\partial V)/(\partial z)]_{d \rightarrow \infty} = -E(d \rightarrow \infty) = 0$ (infinite slab).

Then,

$$c_Q = \kappa \epsilon_0 \frac{\partial}{\partial V_0} \left[\frac{\partial V}{\partial z} \right]_{z=0}. \quad (\text{A2})$$

Hence, the quantum capacitance measures the changing local (top surface) depletion or accumulation profile $[(\partial V)/(\partial z)]_{z=0}$ induced by the applied surface electrical potential V_0 . Given in this form, the quantum capacitance from a 3D semiconductor is conceptually simple to understand but not straightforward to quantify experimentally. We next relate this quantum capacitance to the screening length.

Using the Poisson equation again, we can show that since

$$\frac{\rho(z)}{\kappa \epsilon_0} = \frac{\partial^2 V}{\partial z^2},$$

we can write

$$\int_0^\infty \frac{\rho(z)}{\kappa \epsilon_0} \frac{\partial V}{\partial z} dz = \int_0^\infty \frac{\partial^2 V}{\partial z^2} \frac{\partial V}{\partial z} dz,$$

$$\int_{V(0)}^0 \frac{\rho(V) \partial V}{\kappa \epsilon_0} = -\frac{1}{2} \left(\frac{\partial V}{\partial z} \right)_{z=0}^2.$$

Again, assuming V and $(\partial V)/(\partial z)$ tend to 0 at ∞ , we get

$$\sqrt{2 \int_0^{V(z=0)} \frac{\rho(V) \partial V}{\kappa \epsilon_0}} = \left[\frac{\partial V}{\partial z} \right]_{z=0}$$

with $V(z=0)$ by definition equal to V_0 . Then, the term $[\partial/(\partial V_0)][(\partial V)/(\partial z)]_{z=0}$ in the quantum capacitance can be written as

$$\frac{\partial}{\partial V_0} \left[\frac{\partial V}{\partial z} \right]_{z=0} = \frac{\partial}{\partial V_0} \left[\sqrt{2 \int_0^{V_0} \frac{\rho(V) \partial V}{\kappa \epsilon_0}} \right]$$

$$= \frac{\frac{\partial}{\partial V_0} \int_0^{V_0} \rho(V) \partial V}{\sqrt{2 \kappa \epsilon_0 \int_0^{V_0} \rho(V) \partial V}},$$

$$\frac{\partial}{\partial V_0} \left[\frac{\partial V}{\partial z} \right]_{z=0} = \frac{\rho(V_0)}{\sqrt{2 \kappa \epsilon_0 \int_0^{V_0} \rho(V) \partial V}},$$

or

$$\frac{\partial}{\partial V_0} \left[\frac{\partial V}{\partial z} \right]_{z=0} = \frac{\rho(V_0)}{\kappa \epsilon_0 \left[\frac{\partial V}{\partial z} \right]_{z=0}} = \frac{\rho(V_0)}{\kappa \epsilon_0 E(0)}.$$

Finally, combining this result with Eq. (A2), we get the quantum capacitance

$$c_Q = \frac{\rho(V_0)}{E(0)}. \quad (\text{A3})$$

From Gauss's law, we get

$$\frac{\partial E}{\partial z} = \frac{\rho}{\kappa \epsilon_0}.$$

Integrating from 0 to infinity and assuming E tends to zero at infinity yields

$$\kappa \epsilon_0 E(0) = -e \int_0^\infty n_0 e^{-(z/\lambda)} dz = en_0 \lambda.$$

Here, the charge distribution is assumed to follow an exponential decay into the sample

$$\rho(z) = -en_0 e^{-(z/\lambda)},$$

where n_0 is the charge at $z=0$, and λ is an effective screening length. We get

$$\lambda = \frac{\kappa \epsilon_0 E(0)}{en_0} = \frac{\kappa \epsilon_0 E(0)}{\rho(V_0)}.$$

Then, using Eq. (A3), we get

$$\lambda = \frac{\kappa \epsilon_0}{c_Q^{\text{bulk}}}.$$

Note that here, c_Q^{bulk} is a quantum capacitance related to a 2D compressibility from a charge accumulation or depletion profile. It is related to the 2D density of states of this charging profile. The screening length λ is not the Thomas-Fermi screening length but rather a screening length parameter that varies with the chemical potential and depends on the 2D quantum capacitance of a surface charging or depletion layer. We, thus, derive the dependence of the screening length on the quantum capacitance that we measure experimentally.

APPENDIX B: QUANTUM CAPACITANCE FROM TWO DIRAC SURFACE STATES COUPLED VIA AN INSULATING BULK

A capacitance model accounting for two Dirac surface states coupled via an insulating bulk [Fig. 6(b)] results in the following expression:

$$c_Q(\mu_T) = c_Q^{\text{TTSS}}(\mu_T) + \left(\frac{1}{c_g^{\text{bulk}}} + \frac{1}{c_Q^{\text{BTSS}}(\mu_T)} \right)^{-1}.$$

Here, c_g^{bulk} is the bulk geometric capacitance, and $\mu_T \equiv \varepsilon_F$ is the top-surface chemical potential.

The expression for the quantum capacitance of a single Dirac cone at the top surface [Eq. (5) in the main text] is straightforward to determine,

$$c_Q^{\text{TTSS}}(\mu_T) = \frac{e^2 |\mu_T|}{2\pi(\hbar v_f)^2}, \quad (\text{B1})$$

where v_f is the Fermi velocity.

The expression for the quantum capacitance of a single Dirac cone at the bottom surface is more challenging to extract:

$$c_Q^{\text{BTSS}}(\mu_T) = \frac{e^2 |\mu_B(\mu_T)|}{2\pi(\hbar v_f)^2}.$$

Knowledge of $\mu_B(\mu_T)$ is required. This can be modeled by carefully studying electrochemical equilibrium in a system of two Dirac fluids in parallel, coupled by an insulating capacitive layer.

The electrochemical potential μ^* imposed by the metallic contact ensures equilibrium and allows us to write

$$\mu^* = \mu_T - eV_T + W = \mu_B - eV_B. \quad (\text{B2})$$

Here, $\mu_{T(B)}$ and $V_{T(B)}$ are, respectively, the chemical potential and the electric potential at the top or bottom surface, and W is a work function term that includes contributions that allow band misalignment such as band bending and surface charging due to impurities which essentially lead to a band offset between the top and bottom surface Dirac point.

The 2D carrier density n_{2D} as a function of chemical potential μ for nonspin degenerate Dirac surface states can be written as

$$n = \text{sgn}(\mu) \frac{\mu^2}{4\pi(\hbar v_f)^2}. \quad (\text{B3})$$

The charge density is simply given by $\rho = -ne$.

We now apply Gauss's law to find an expression for the charge density at the top and bottom interfaces.

For the bottom surface, we have

$$c_g^{\text{bulk}}(V_B - V_T) = -en_B. \quad (\text{B4})$$

c_{TG} is the geometric top gate capacitance, and $n_{T(B)}$ is the carrier density of the top or bottom surface. V_G is the gate voltage. We can now proceed and compute the variation of the quantum capacitance as a function of the chemical potential of the top surface.

By plugging into Eq. (B4), the expression for V_T and V_B determined from Eq. (B2) and that of n_T and n_B from Eq. (B3), we get

$$c_g^{\text{bulk}}(\mu_B - \mu_T - W) = -e^2 \text{sgn}(\mu_B) \frac{\mu_B^2}{4\pi(\hbar v_f)^2}.$$

We then set up a second-degree equation to extract μ_B as a function of μ_T ,

$$\frac{4\pi(\hbar v_f)^2}{e^2} c_g^{\text{bulk}}(\mu_B - \mu_T - W) + \text{sgn}(\mu_B) \mu_B^2 = 0.$$

We get four solutions, two of which are inconsistent with the sign of μ_B .

For $\mu_B > 0$,

$$\mu_B = \frac{2\pi(\hbar v_f)^2}{e^2} c_g^{\text{bulk}} \left(-1 \pm \sqrt{1 + \frac{e^2(\mu_T + W)}{\pi(\hbar v_f)^2 c_g^{\text{bulk}}}} \right).$$

Only the solution with the + sign satisfies $\mu_B > 0$.

Similar for $\mu_B < 0$, we get only one satisfactory solution:

$$\mu_B = \frac{2\pi(\hbar v_f)^2}{e^2} c_g^{\text{bulk}} \left(1 - \sqrt{1 + \frac{e^2(\mu_T + W)}{\pi(\hbar v_f)^2 c_g^{\text{bulk}}}} \right).$$

Finally, we have μ_B as a function of μ_T :

$$\mu_B(\mu_T) = \pm \frac{2\pi(\hbar v_f)^2}{e^2} c_g^{\text{bulk}} \left(1 - \sqrt{1 + \frac{e^2(\mu_T + W)}{\pi(\hbar v_f)^2 c_g^{\text{bulk}}}} \right).$$

This expression can then be used to find c_Q^{BTSS} :

$$c_Q^{\text{BTSS}}(\mu_T) = c_g^{\text{bulk}} \left(-1 + \sqrt{1 + \frac{e^2(\mu_T + W)}{\pi(\hbar v_f)^2 c_g^{\text{bulk}}}} \right) > 0.$$

We finally obtain the expression for the total quantum capacitance:

$$c_Q(\mu_T) = c_Q^{\text{TTSS}}(\mu_T) + \frac{c_g^{\text{bulk}} c_Q^{\text{BTSS}}(\mu_T)}{c_g^{\text{bulk}} + c_Q^{\text{BTSS}}(\mu_T)},$$

$$c_Q(\mu_T) = c_Q^{\text{TTSS}}(\mu_T) + c_g^{\text{bulk}} \left[1 - \frac{1}{\left(\sqrt{1 + \frac{e^2(\mu_T + W)}{\pi(\hbar v_f)^2 c_g^{\text{bulk}}}} \right)} \right].$$

Finally, replacing μ_T by ε_F to keep a coherent notation, we get

$$c_Q(\mu_T) = \frac{e^2 |\varepsilon_F|}{2\pi(\hbar v_f)^2} + c_g^{\text{bulk}} \left[1 - \frac{1}{\left(\sqrt{1 + \frac{e^2 |\varepsilon_F + W|}{\pi(\hbar v_f)^2 c_g^{\text{bulk}}}} \right)} \right]. \quad (\text{B5})$$

We highlight the simplicity of this model from an experimental viewpoint, since most parameters can be determined independently from previous measurements. The only adjustable parameter is the band offset W .

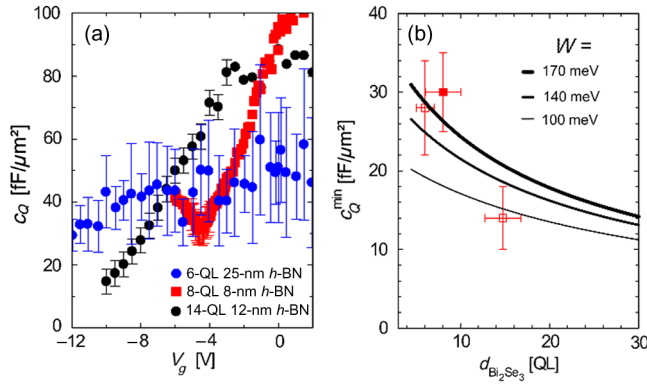


FIG. 7. (a) Quantum capacitance versus gate voltage for the three Bi_2Se_3 samples. (b) Smallest c_Q measured in each respective sample. A full square indicates the sample for which we observe the Dirac point feature. An empty square is used for the other. The thickness (horizontal) error bar accounts for the sample roughness. Solid lines represent the variation of Eq. (8) versus the thickness for different values of W .

APPENDIX C: THICKNESS DEPENDENCE

We also measure two additional MITI devices having, respectively, thinner and thicker Bi_2Se_3 . The device characteristics are summarized in Table II. Both devices exhibit a capacitance that varies with the voltage. The quantum capacitance is extracted in each case using the analysis described in the main text. We do not observe a capacitance minimum in those devices. The quantum capacitance versus gate-voltage curve for the 6-QL and 14-QL samples are shown in Fig. 7(a) and compared to that of the 8-QL sample. The experimental error bars are quite large in the 6 QLs near $V = 0$ since the top h -BN used for this sample is quite thick (25 nm) and has a small geometrical capacitance. The quantum-capacitance measurement is thus less precise in this sample.

This comparison allows us to get an idea about how the capacitance offset depends on the thickness. Recall in Eq. (9), the offset is shown to depend on both c_g^{bulk} and W the Fermi energy offset. c_g^{bulk} is inversely proportional to the Bi_2Se_3 thickness. In Fig. 7(b), we compare the smallest quantum-capacitance values measured for each sample. The capacitance minima are plotted versus the sample thickness and compared to the variation of Eq. (9) with the sample thickness and W . The data suggest that varying the thickness yields a changing c_g^{bulk} and W . In the thicker

TABLE II. Sample list showing corresponding Bi_2Se_3 and h -BN thicknesses.

	Bi_2Se_3 thickness (QLs)	h -BN thickness (nm)
Sample 1	8	8
Sample 2	14	12
Sample 3	6	25

sample, even though the bottom surface is further decoupled from the top gate, its influence on the quantum capacitance is also smaller. This is due to c_g^{bulk} becoming smaller when the sample thickness increases [see Eq. (9)]. This agrees with the fact the capacitance offset observed in HgTe (approximately 70 nm) [21] is smaller than that measured in the Bi_2Se_3 8 QLs.

While we cannot draw more conclusions from this analysis, we are motivated to conduct further work on the thickness dependence and the question of capacitive top-bottom coupling.

- [1] F. D. M. Haldane, Model for a Quantum Hall Effect without Landau Levels: Condensed-Matter Realization of the ‘‘Parity Anomaly,’’ *Phys. Rev. Lett.* **61**, 2015 (1988).
- [2] Q. Niu, D. J. Thouless, and Y. S. Wu, Quantized Hall conductance as a topological invariant, *Phys. Rev. B* **31**, 3372 (1985).
- [3] C. L. Kane and E. J. Mele, Quantum Spin Hall Effect in Graphene, *Phys. Rev. Lett.* **95**, 226801 (2005).
- [4] B. A. Bernevig, T. L. Hughes, and S.-C. Zhang, Quantum spin Hall effect and topological phase transition in HgTe quantum wells, *Science* **314**, 1757 (2006).
- [5] M. Z. Hasan and C. L. Kane, Colloquium: Topological insulators, *Rev. Mod. Phys.* **82**, 3045 (2010).
- [6] X.-L. Qi and S.-C. Zhang, Topological insulators and superconductors, *Rev. Mod. Phys.* **83**, 1057 (2011).
- [7] Y. Ando, Topological insulator materials, *J. Phys. Soc. Jpn.* **82**, 102001 (2013).
- [8] Y. Ando and L. Fu, Topological crystalline insulators and topological superconductors: From concepts to materials, *Annu. Rev. Condens. Matter Phys.* **6**, 361 (2015).
- [9] C.-Z. Chang, W. Zhao, D. Y. Kim, H. Zhang, B. A. Assaf, D. Heiman, S.-C. Zhang, C. Liu, M. H. W. Chan, and J. S. Moodera, High precision realization of robust quantum anomalous Hall state in a hard ferromagnetic topological insulator, *Nat. Mater.* **14**, 473 (2015).
- [10] C.-Z. Chang *et al.*, Experimental observation of the quantum anomalous Hall effect in a magnetic topological insulator, *Science* **340**, 167 (2013).
- [11] E. Bocquillon, R. S. Deacon, J. Wiedenmann, P. Leubner, T. M. Klapwijk, C. Brüne, K. Ishibashi, H. Buhmann, and L. W. Molenkamp, Gapless Andreev bound states in quantum spin Hall insulator HgTe, *Nat. Nanotechnol.* **12**, 137 (2017).
- [12] L. Wu, M. Salehi, N. Koirala, J. Moon, S. Oh, and N. P. Armitage, Quantized Faraday and Kerr rotation and axion electrodynamics of 3D topological insulator, *Science* **354**, 1124 (2016).
- [13] A. Shuvaev, V. Dziom, Z. D. Kvon, N. N. Mikhailov, and A. Pimenov, Universal Faraday Rotation in HgTe Wells with Critical Thickness, *Phys. Rev. Lett.* **117**, 117401 (2016).
- [14] A. R. Mellnik, J. S. Lee, a. Richardella, J. L. Grab, P. J. Mintun, M. H. Fischer, a. Vaezi, a. Manchon, E.-a. Kim, N. Samarth, and D. C. Ralph, Spin-transfer torque generated by a topological insulator, *Nature (London)* **511**, 449 (2014).
- [15] M. Jamali, J. S. Lee, J. S. Jeong, F. Mahfouzi, Y. Lv, Z. Zhao, B. K. Nikolić, K. A. Mkhoyan, N. Samarth, and

- J. Wang, Giant spin pumping and inverse spin Hall effect in the presence of surface and bulk spin-orbit coupling of topological insulator Bi_2Se_3 , *Nano Lett.* **15**, 7126 (2015).
- [16] J. Han, A. Richardella, S. A. Siddiqui, J. Finley, N. Samarth, and L. Liu, Room-Temperature Spin-Orbit Torque Switching Induced by a Topological Insulator, *Phys. Rev. Lett.* **119**, 077702 (2017).
- [17] E. Pallecchi, a. C. Betz, J. Chaste, G. Fève, B. Huard, T. Kontos, J.-M. Berroir, and B. Plaças, Transport scattering time probed through rf admittance of a graphene capacitor, *Phys. Rev. B* **83**, 125408 (2011).
- [18] Q. Wilmart, A. Inhofer, M. Boukhicha, W. Yang, M. Rosticher, P. Morfin, N. Garroum, G. Fève, J.-M. Berroir, and B. Plaças, Contact gating at GHz frequency in graphene, *Sci. Rep.* **6**, 21085 (2016).
- [19] A. C. Betz, S. H. Jhang, E. Pallecchi, R. Ferreira, G. Fève, J.-M. Berroir, and B. Plaças, Supercollision cooling in undoped graphene, *Nat. Phys.* **9**, 109 (2013).
- [20] Y.-M. Lin, C. Dimitrakopoulos, K. A. Jenkins, D. B. Farmer, H.-Y. Chiu, A. Grill, and P. Avouris, 100-GHz transistors from wafer-scale epitaxial graphene, *Science* **327**, 662 (2010).
- [21] A. Inhofer, S. Tchoumakov, B. A. Assaf, G. Fève, J. M. Berroir, V. Jouffrey, D. Carpentier, M. O. Goerbig, B. Plaças, K. Bendias, D. M. Mahler, E. Bocquillon, R. Schlereth, C. Brüne, H. Buhmann, and L. W. Molenkamp, Observation of Volkov-Pankratov states in topological HgTe heterojunctions using high frequency compressibility, *Phys. Rev. B* **96**, 195104 (2017).
- [22] A. Inhofer, Ph.D. thesis, Ecole Normale Supérieure, 2017.
- [23] J. G. Analytis, J.-H. Chu, Y. Chen, F. Corredor, R. D. McDonald, Z. X. Shen, and I. R. Fisher, Bulk Fermi surface coexistence with Dirac surface state in Bi_2Se_3 : A comparison of photoemission and Shubnikov-de Haas measurements, *Phys. Rev. B* **81**, 205407 (2010).
- [24] M. Neupane *et al.*, Observation of quantum-tunnelling-modulated spin texture in ultrathin topological insulator Bi_2Se_3 films, *Nat. Commun.* **5**, 3841 (2014).
- [25] K. He, Y. Zhang, K. He, C. Chang, C. Song, L. Wang, X. Chen, J. Jia, Z. Fang, X. Dai, W. Shan, S. Shen, Q. Niu, X. Qi, S. Zhang, X.-C. Ma, and Q.-K. Xue, Crossover of the three-dimensional topological insulator Bi_2Se_3 to the two-dimensional limit, *Nat. Phys.* **6**, 584 (2010).
- [26] S. Xu, Y. Han, X. Chen, Z. Wu, L. Wang, T. Han, W. Ye, H. Lu, G. Long, Y. Wu, J. Lin, Y. Cai, K. M. Ho, Y. He, and N. Wang, van der Waals epitaxial growth of atomically thin Bi_2Se_3 and thickness-dependent topological phase transition, *Nano Lett.* **15**, 2645 (2015).
- [27] P. Gehring, B. F. Gao, M. Burghard, and K. Kern, Growth of $\text{Bi}_2\text{Te}_2\text{Se}$ nanoplatelets on hBN sheets by van der Waals epitaxy, *Nano Lett.* **12**, 5137 (2012).
- [28] T. Taniguchi and K. Watanabe, Synthesis of high-purity boron nitride single crystals under high pressure by using Ba-BN solvent, *J. Cryst. Growth* **303**, 525 (2007).
- [29] C. R. Dean, a. F. Young, I. Meric, C. Lee, L. Wang, S. Sorgenfrei, K. Watanabe, T. Taniguchi, P. Kim, K. L. Shepard, and J. Hone, Boron nitride substrates for high-quality graphene electronics, *Nat. Nanotechnol.* **5**, 722 (2010).
- [30] W. Dang, H. Peng, H. Li, P. Wang, and Z. Liu, Epitaxial heterostructures of ultrathin topological insulator nanoplate and graphene, *Nano Lett.* **10**, 2870 (2010).
- [31] A. S. Mayorov, R. V. Gorbachev, S. V. Morozov, L. Britnell, R. Jalil, L. a. Ponomarenko, P. Blake, K. S. Novoselov, K. Watanabe, T. Taniguchi, and a. K. Geim, Micrometer-scale ballistic transport in encapsulated graphene at room temperature, *Nano Lett.* **11**, 2396 (2011).
- [32] M. H. D. Guimarães, P. J. Zomer, J. Ingla-Aynés, J. C. Brant, N. Tombros, and B. J. van Wees, Controlling Spin Relaxation in Hexagonal BN-Encapsulated Graphene with a Transverse Electric Field, *Phys. Rev. Lett.* **113**, 086602 (2014).
- [33] S. Xu, Z. Wu, H. Lu, Y. Han, G. Long, X. Chen, T. Han, W. Ye, Y. Wu, J. Lin, J. Shen, Y. Cai, Y. He, F. Zhang, R. Lortz, C. Cheng, and N. Wang, Universal low-temperature Ohmic contacts for quantum transport in transition metal dichalcogenides, *2D Mater.* **3**, 021007 (2016).
- [34] X. Chen, Y. Wu, Z. Wu, Y. Han, S. Xu, L. Wang, W. Ye, T. Han, Y. He, Y. Cai, and N. Wang, High-quality sandwiched black phosphorus heterostructure and its quantum oscillations, *Nat. Commun.* **6**, 7315 (2015).
- [35] K. S. Novoselov, A. Mishchenko, A. Carvalho, and A. H. Castro Neto, 2D materials and van der Waals heterostructures, *Science* **353**, aac9439 (2016).
- [36] Z. Fei, T. Palomaki, S. Wu, W. Zhao, X. Cai, B. Sun, P. Nguyen, J. Finney, X. Xu, and D. H. Cobden, Edge conduction in monolayer WTe_2 , *Nat. Phys.* **13**, 677 (2017).
- [37] J. I.-J. Wang, Y. Yang, Y.-A. Chen, K. Watanabe, T. Taniguchi, H. O. H. Churchill, and P. Jarillo-Herrero, Electronic transport of encapsulated graphene and WSe_2 devices fabricated by pick-up of prepatterned hBN, *Nano Lett.* **15**, 1898 (2015).
- [38] D. M. Pozar, *Microwave Engineering*, 3rd ed. (Wiley, New York, 2005).
- [39] C. N. Berglund, Surface states at steam-grown silicon-silicon dioxide interfaces, *IEEE Trans. Electron Devices* **ED-13**, 701 (1966).
- [40] Y. Xia, D. Qian, D. Hsieh, L. Wray, A. Pal, H. Lin, A. Bansil, D. Grauer, Y. S. Hor, R. J. Cava, and M. Z. Hasan, Observation of a large-gap topological-insulator class with a single Dirac cone on the surface, *Nat. Phys.* **5**, 398 (2009).
- [41] M. Orlita, B. a. Piot, G. Martinez, N. K. S. Kumar, C. Faugeras, M. Potemski, C. Michel, E. M. Hankiewicz, T. Brauner, Č. Drašar, S. Schreyeck, S. Grauer, K. Brunner, C. Gould, C. Brüne, and L. W. Molenkamp, Magneto-Optics of Massive Dirac Fermions in Bulk Bi_2Se_3 , *Phys. Rev. Lett.* **114**, 186401 (2015).
- [42] H. He, B. Li, H. Liu, X. Guo, Z. Wang, M. Xie, and J. Wang, High-field linear magneto-resistance in topological insulator Bi_2Se_3 thin films, *Appl. Phys. Lett.* **100**, 032105 (2012).
- [43] L. Wu, M. Brahlek, R. Valdés Aguilar, a. V. Stier, C. M. Morris, Y. Lubashevsky, L. S. Bilbro, N. Bansal, S. Oh, and N. P. Armitage, A sudden collapse in the transport lifetime across the topological phase transition in $((\text{Bi}_{1-x}\text{In}_x)_2\text{Se}_3)$, *Nat. Phys.* **9**, 410 (2013).
- [44] J. Son, K. Banerjee, M. Brahlek, N. Koirala, S.-K. Lee, J.-H. Ahn, S. Oh, and H. Yang, Defect-induced negative magneto-resistance and surface state robustness in the topological insulator BiSbTeSe_2 , *Appl. Phys. Lett.* **103**, 213114 (2013).

- [45] L. Veyrat, F. Iacovella, J. Dufouleur, C. Nowka, H. Funke, M. Yang, W. Escoffier, M. Goiran, B. Eichler, O. G. Schmidt, B. Büchner, S. Hampel, and R. Giraud, Band bending inversion in Bi_2Se_3 nanostructures, *Nano Lett.* **15**, 7503 (2015).
- [46] A. A. Taskin, S. Sasaki, K. Segawa, and Y. Ando, Achieving surface quantum oscillations in topological insulator thin films of Bi_2Se_3 , *Adv. Mater.* **24**, 5581 (2012).
- [47] H. Steinberg, J.-B. Laloë, V. Fatemi, J. S. Moodera, and P. Jarillo-Herrero, Electrically tunable surface-to-bulk coherent coupling in topological insulator thin films, *Phys. Rev. B* **84**, 233101 (2011).
- [48] H. Liu, S. Liu, Y. Yi, H. He, and J. Wang, Shubnikov–de Haas oscillations in n and p type Bi_2Se_3 flakes, *2D Mater.* **2**, 045002 (2015).
- [49] N. Koirala, M. Brahlek, M. Salehi, L. Wu, J. Dai, J. Waugh, T. Nummy, M. G. Han, J. Moon, Y. Zhu, D. Dessau, W. Wu, N. P. Armitage, and S. Oh, Record surface state mobility and quantum Hall effect in topological insulator thin films via interface engineering, *Nano Lett.* **15**, 8245 (2015).
- [50] J. Y. Park, G.-H. Lee, J. Jo, A. K. Cheng, H. Yoon, K. Watanabe, T. Taniguchi, M. Kim, P. Kim, and G.-C. Yi, Molecular beam epitaxial growth and electronic transport properties of high quality topological insulator Bi_2Se_3 thin films of hexagonal boron nitride, *2D Mater.* **3**, 035029 (2016).
- [51] D. Kim, S. Cho, N. P. Butch, P. Syers, K. Kirshenbaum, S. Adam, J. Paglione, and M. S. Fuhrer, Surface conduction of topological Dirac electrons in bulk insulating Bi_2Se_3 , *Nat. Phys.* **8**, 459 (2012).
- [52] D. Hsieh, Y. Xia, D. Qian, L. Wray, J. H. Dil, F. Meier, J. Osterwalder, L. Patthey, J. G. Checkelsky, N. P. Ong, A. V. Fedorov, H. Lin, A. Bansil, D. Grauer, Y. S. Hor, R. J. Cava, and M. Z. Hasan, A tunable topological insulator in the spin helical Dirac transport regime, *Nature (London)* **460**, 1101 (2009).
- [53] G. L. Yu, R. Jalil, B. Belle, A. S. Mayorov, P. Blake, F. Schedin, S. V. Morozov, L. a. Ponomarenko, F. Chiappini, S. Wiedmann, U. Zeitler, M. I. Katsnelson, a. K. Geim, K. S. Novoselov, and D. C. Elias, Interaction phenomena in graphene seen through quantum capacitance, *Proc. Natl. Acad. Sci. U.S.A.* **110**, 3282 (2013).
- [54] M. Bianchi, D. Guan, S. Bao, J. Mi, B. B. Iversen, P. D. C. King, and P. Hofmann, Coexistence of topological state and a two-dimensional electron gas on the surface of Bi_2Se_3 , *Nat. Commun.* **1**, 128 (2010).
- [55] N. P. Butch, K. Kirshenbaum, P. Syers, A. B. Sushkov, G. S. Jenkins, H. D. Drew, and J. Paglione, Strong surface scattering in ultrahigh mobility Bi_2Se_3 topological insulator crystals, *Phys. Rev. B* **81**, 241301 (2010).
- [56] H. Köhler and C. R. Becker, Optically active lattice vibrations in Bi_2Se_3 , *Phys. Status Solidi* **61**, 533 (1974).
- [57] V. Fatemi, B. Hunt, H. Steinberg, S. L. Eltinge, F. Mahmood, N. P. Butch, K. Watanabe, T. Taniguchi, N. Gedik, R. C. Ashoori, and P. Jarillo-Herrero, Electrostatic Coupling between Two Surfaces of a Topological Insulator Nanodevice, *Phys. Rev. Lett.* **113**, 206801 (2014).
- [58] Y. Shao, K. W. Post, J.-S. Wu, S. Dai, A. J. Frenzel, A. R. Richardella, J. S. Lee, N. Samarth, M. M. Fogler, A. V. Balatsky, D. E. Kharzeev, and D. N. Basov, Faraday rotation due to surface states in the topological insulator $(\text{Bi}_{1-x}\text{Sb}_x)_2\text{Te}_3$, *Nano Lett.* **17**, 980 (2017).
- [59] D. A. Kozlov, D. Bauer, J. Ziegler, R. Fischer, M. L. Savchenko, Z. D. Kvon, N. N. Mikhailov, S. A. Dvoretzky, and D. Weiss, Probing Quantum Capacitance in a 3D Topological Insulator, *Phys. Rev. Lett.* **116**, 166802 (2016).
- [60] H. Preier, Recent advances in lead-chalcogenide diode lasers, *Appl. Phys.* **20**, 189 (1979).
- [61] B. A. Assaf, T. Phuphachong, V. V. Volobuev, G. Bauer, G. Springholz, L.-A. de Vaulchier, and Y. Guldner, Magneto-optical determination of a topological index, *npj Quantum Mater.* **2**, 26 (2017).